

# **Electrosynthesis of hydroxylamine *via* plasma-electrochemical cascade pathway using the air and water as raw materials**

Xiangdong Kong<sup>1,3</sup>, Jie Ni<sup>1,3</sup>, Zhimin Song<sup>1</sup>, Zhengwu Yang<sup>1</sup>, Jiana Zheng<sup>1</sup>, Zifan Xu<sup>1</sup>, Lang Qin,<sup>1</sup> Hongliang Li<sup>1</sup>, Zhigang Geng<sup>1,\*</sup>, Jie Zeng<sup>1,2,\*</sup>

<sup>1</sup>Hefei National Research Center for Physical Sciences at the Microscale, Key Laboratory of Strongly-Coupled Quantum Matter Physics of Chinese Academy of Sciences, Key Laboratory of Surface and Interface Chemistry and Energy Catalysis of Anhui Higher Education Institutes, Department of Chemical Physics, University of Science and Technology of China, Hefei, Anhui 230026, P. R. China

<sup>2</sup>School of Chemistry & Chemical Engineering, Anhui University of Technology, Ma'anshan, Anhui 243002, P. R. China

<sup>3</sup>These authors contributed equally to this work.

\*Corresponding authors. E-mail: gengzg@ustc.edu.cn (Z.G.); zengj@ustc.edu.cn (J.Z.)

## Abstract

The ambient air contains abundant nitrogenous resources that are essential for amine synthesis. Unfortunately, the inert  $N_2$  with stable  $N\equiv N$  obstructs the direct synthesis of active nitrogenous compounds from the ambient air. Herein, we developed a sustainable plasma-electrochemical cascade pathway (PECP) powered by renewable electricity for electrosynthesizing one of the active nitrogenous compounds, hydroxylamine ( $NH_2OH$ ), directly from the ambient air and  $H_2O$ . During the PECP, we obtained the nitrate ( $NO_3^-$ ) solution with a concentration of as high as 120.1 mM. Subsequently, the  $NO_3^-$  solution was selectively electroreduced to  $NH_2OH$  over Bi-based catalyst. Notably, the faradaic efficiency for  $NH_2OH$  reached 81.0% at -1.0 V versus reversible hydrogen electrode. Moreover, we also obtained a state-of-the-art yield rate for  $NH_2OH$  of  $713.1 \mu mol cm^{-2} h^{-1}$  with selectivity for  $NH_2OH$  of 99.3%. Theoretical studies revealed that the Bi(012) facet displayed weaker adsorption energy for the adsorbed  $NH_2OH$  intermediate ( $*NH_2OH$ ) in comparison with other kinds of metallic facets, indicating that the Bi catalyst facilitates the desorption of  $*NH_2OH$ . Meanwhile, the desorption of  $*NH_2OH$  was much more favorable than the dissociation of  $*NH_2OH$  on the Bi(012) facet, resulting in the highly selective formation of  $NH_2OH$  over Bi-based catalysts.

**Keywords:** utilization of ambient air, electrosynthesis of  $NH_2OH$ , plasma fixation of  $N_2$ ,  $NO_3^-$  electroreduction.

## Introduction

Hydroxylamine ( $\text{NH}_2\text{OH}$ ), as an important nitrogenous feedstock with high reactivity, has been widely applied for the synthesis of nitrogen-containing compounds in the chemical, agrochemical, and pharmaceutical fields<sup>1-6</sup>. The traditionally industrial methods for the synthesis of  $\text{NH}_2\text{OH}$  include the Raschig method, nitric monoxide ( $\text{NO}$ ) reduction method, and nitric acid ( $\text{HNO}_3$ ) reduction method (Fig. 1a)<sup>7-9</sup>. Nonetheless, the Raschig method employs both highly corrosive and polluted sulfur dioxide as the reductant with producing a large amount of  $(\text{NH}_4)_2\text{SO}_4$  as the by-product. As for both  $\text{NO}$  and  $\text{HNO}_3$  reduction methods,  $\text{H}_2$  derived from the petrochemical process and noble metal materials ( $\text{Pt}$ ,  $\text{Pd}$ ,  $\text{Ru}$ , and  $\text{Rh}$ ) have been used as proton source and catalysts, respectively, greatly increasing the cost for  $\text{NH}_2\text{OH}$  production<sup>9-11</sup>. Although other paths such as acetoxime method, methyl-ethyl ketone method, and hydrogen peroxide oxidation method have been developed for the potential synthesis of  $\text{NH}_2\text{OH}$ <sup>12-15</sup>, they have also been confronted with the high cost of reactants or the low yield for  $\text{NH}_2\text{OH}$  production (Fig. 1b). Moreover, it is worth noting that the nitrogen sources for all these traditionally synthetic methods for  $\text{NH}_2\text{OH}$  originate from the energy-intensive Haber-Bosch process, leading to serious carbon footprint and energy consumption issues<sup>16-18</sup>. In order to circumvent the aforementioned drawbacks, it is of pivotal significance to exploit both more practical and sustainable alternatives for  $\text{NH}_2\text{OH}$  synthesis.

In this work, we developed a plasma-electrochemical cascade pathway (PECP) for the renewable  $\text{NH}_2\text{OH}$  electrosynthesis from the ambient air and  $\text{H}_2\text{O}$  (Fig. 1c). Such PECP included the preparation of nitrate ( $\text{NO}_3^-$ ) from the ambient air by plasma synthesis and the production of  $\text{NH}_2\text{OH}$  towards  $\text{NO}_3^-$  electroreduction. In contrast to the traditionally synthetic paths, the electrosynthesis driven by renewable electricity using both green and abundant  $\text{H}_2\text{O}$  as proton source paves a promising avenue for the sustainable production of  $\text{NH}_2\text{OH}$ . To overcome the limitation of the extremely low reactivity for the direct  $\text{N}_2$  electrochemical activation<sup>19-21</sup>, we exploited a homemade plasma discharge device for the highly efficient  $\text{N}_2$  activation into the oxynitride ( $\text{NO}_x$ ) by straightly using the ambient air as feeding gas. After steadily absorbing the  $\text{NO}_x$  with  $\text{H}_2\text{O}$  for 30 min, we obtained the  $\text{NO}_3^-$  solution with the concentration of as high as 120.1 mM. Subsequently, the  $\text{NO}_3^-$  solution was selectively electroreduced to  $\text{NH}_2\text{OH}$  using Bi nanoparticles loaded on carbon fiber paper (denoted as Bi NPs/CFP) as the catalyst. At applied potential of -1.0 V versus reversible hydrogen electrode (vs. RHE), Bi NPs/CFP exhibited a

faradaic efficiency (FE) for  $\text{NH}_2\text{OH}$  of 81.0%. Notably, a yield rate for  $\text{NH}_2\text{OH}$  of  $713.1 \mu\text{mol cm}^{-2} \text{ h}^{-1}$  was achieved over Bi NPs/CFP at  $-1.2 \text{ V}$  vs. RHE. Based on density functional theory (DFT) calculations, the Bi(012) facet displayed a weaker adsorption energy ( $E_{\text{ads}}$ ) for the adsorbed  $\text{NH}_2\text{OH}$  intermediate ( $^*\text{NH}_2\text{OH}$ ) in comparison with other kinds of metallic facets, suggesting that Bi catalyst brings benefit to the desorption of  $^*\text{NH}_2\text{OH}$ . Meanwhile, the desorption of  $^*\text{NH}_2\text{OH}$  was much more favorable than the dissociation of  $^*\text{NH}_2\text{OH}$  on the Bi(012) facet, resulting in the highly selective formation of  $\text{NH}_2\text{OH}$  towards  $\text{NO}_3^-$  electroreduction.

## Results and discussion

**Plasma synthesis of  $\text{NO}_3^-$  from the ambient air and  $\text{H}_2\text{O}$ .** As indicated by the reaction mechanism and previous reports on the discharge activation of  $\text{N}_2$ <sup>22-24</sup>, it is of vital importance to increase the collision probability between N and O radicals for improving the yield rate of  $\text{NO}_x$ . Because the dissociation of inert  $\text{N}_2$  into N radicals take place within the energy-concentrated region of the plasma discharge device, the overlapping zone between the electric arc and the ambient air is positively correlated with the activation rate of  $\text{N}_2$ . Hence, we designed a plasma discharge device equipped with multiple parallel tips to enlarge the overlapping zone for the efficient activation of  $\text{N}_2$  (Supplementary Fig. 1). Typically, a high-voltage power supply with an input alternating current (AC) voltage of 50 V was adopted to generate an output AC voltage of 10 kV between the tips. To verify the feasibility of  $\text{N}_2$  plasma fixation from ambient air on the homemade plasma discharge device, we performed a qualitative analysis. When gaseous substances produced by the plasma discharge were purged into the aqueous absorbent containing 0.02 mM methyl orange, the absorbent gradually turned from light yellow to salmon pink within 30 s (Fig. 2, a, b, and Supplementary Video). In contrast, when the ambient air was directly bubbled into the absorbent, no significant change was observed for the color of the absorbent during the absorption time of 10 min (Supplementary Fig. 2). These results suggested that the acidic  $\text{NO}_x$  produced from the plasma discharge was absorbed in aqueous solution to form  $\text{HNO}_3$ .

To evaluate the performance for  $\text{N}_2$  fixation using the plasma discharge device, we quantified the yield of  $\text{NO}_3^-$ . After the absorption of gaseous products in 30 mL of  $\text{H}_2\text{O}$ , the concentration for  $\text{NO}_3^-$  was analyzed by ion chromatography. The flow rate of the ambient air

was a key parameter for optimizing the efficiency of  $\text{N}_2$  fixation. Fig. 2c shows the concentration for  $\text{NO}_3^-$  after the 5-min plasma discharge under various flow rates of the ambient air. The concentrations for  $\text{NO}_3^-$  were monotonically increased when the flow rates of the ambient air were modulated from 20 to 200 standard cubic centimeter per minute (SCCM). Under the flow rate of 200 SCCM, the concentration for  $\text{NO}_3^-$  reached as high as 20.3 mM. To meet the requirement of the high-yield preparation of  $\text{NO}_3^-$ , we chose the flow rate of 200 SCCM as the optimum condition for the continuous discharge process. As shown in Fig. 2d, the concentrations for  $\text{NO}_3^-$  were almost linearly accumulated in 30 mL of absorbent after continuous discharge for various times. Notably, the concentration for  $\text{NO}_3^-$  reached as high as 120.1 mM for 30 min. We further conducted the cyclic stability tests on the plasma discharge device. Each cycle was continuously discharged for 30 min. During 20 cyclic stability tests, the concentrations for  $\text{NO}_3^-$  in the absorbent were always higher than 115.3 mM (Fig. 2e). The as-obtained aqueous  $\text{NO}_3^-$  solution can be directly fed for the  $\text{NO}_3^-$  electroreduction process.

**$\text{NO}_3^-$  electroreduction into  $\text{NH}_2\text{OH}$ .** Bi NPs/CFP was adopted as the catalyst towards  $\text{NO}_3^-$  electroreduction. Typically, Bi NPs/CFP was obtained *via* the magnetron sputtering of Bi disk on CFP with direct current deposition. As revealed by the scanning electron microscope (SEM) measurements (Fig. 3a and Supplementary Fig. 3), Bi nanoparticles were closely packed on the surface of CFP. The SEM images of the cross-sectional Bi NPs/CFP showed a clear interface between CFP and the layer the Bi nanoparticles (Supplementary Fig. 4). The magnified SEM image of the cross-sectional Bi NPs/CFP suggested that the thickness for the layer of Bi nanoparticles was around 730 nm (Fig. 3b). Based on the SEM energy dispersive X-ray (EDX) elemental mapping analysis, the layered-stack structure was also verified by the distinct elemental distributions (Fig. 3c). As shown by the high-angle annular dark field scanning transmission electron microscope (HAADF-STEM) measurement, the interplanar spacing of 0.328 nm for an individual Bi nanoparticle was assigned to (012) facet of metallic Bi (Fig. 3d). In the X-ray diffraction (XRD) spectra, except for the characteristic peaks of CFP, the new peaks at  $22.5^\circ$ ,  $27.2^\circ$ ,  $38.0^\circ$ ,  $39.6^\circ$ ,  $44.6^\circ$ ,  $45.9^\circ$ , and  $59.3^\circ$  were indexed to the (003), (012), (104), (110), (015), (006), and (107) facets of hexagonal Bi (JCPDS No. 41-1246), respectively (Fig. 3e). As shown by Raman spectra, the characteristic peaks at  $70.5$  and  $97.0\text{ cm}^{-1}$  for Bi NPs/CFP were attributed to the  $E_g$  and  $A_{1g}$  stretching modes of the metallic Bi-Bi bond, respectively (Fig. 3f). Supplementary Fig.

5 shows the X-ray spectroscopy (XPS) spectra. Bi NPs/CFP exhibited two peaks at 162.4 and 157.0 eV in the Bi 4f XPS spectrum, assigned to the  $4f_{5/2}$  and  $4f_{7/2}$  of  $\text{Bi}^0$  species, respectively. By contrast, no obvious signal was detected in the Bi 4f XPS spectrum of CFP.

The  $\text{NO}_3^-$  electroreduction measurements were carried out in an H cell using 0.5 M  $\text{H}_2\text{SO}_4$  solution containing 0.1 M  $\text{NO}_3^-$  as the catholyte. The chronoamperometry electrolysis was conducted to quantitatively analyze the catalytic performance of  $\text{NO}_3^-$  electroreduction. During  $\text{NO}_3^-$  electroreduction, an argon (Ar) stream with a flow rate of 20 SCCM was used as the shielding gas to insulate the catholyte from the air. Meanwhile, the gaseous products were carried out by Ar stream for quantification *via* an online gas chromatography (GC). To eliminate the interference of the O-H groups in  $\text{H}_2\text{O}$  to the N-H groups in  $\text{NH}_2\text{OH}$ , we adopted an excess amount of glyoxylic acid ( $\text{C}_2\text{H}_2\text{O}_3$ ) to capture  $\text{NH}_2\text{OH}$  *via* a spontaneous oximation process. As determined by  $^1\text{H}$  nuclear magnetic resonance (NMR) measurements,  $\text{NH}_2\text{OH}$  was quantified based on the C-H group of glyoxylic acid oxime ( $\text{C}_2\text{H}_3\text{NO}_3$ ) (Supplementary Fig. 6). Besides,  $\text{NH}_3$  was also quantitatively analyzed by  $^1\text{H}$  NMR. At all applied potential from -0.6 to -1.2 V vs. RHE,  $\text{NH}_2\text{OH}$  was determined as the predominant product for  $\text{NO}_3^-$  electroreduction over Bi NPs/CFP (Fig. 4a and Supplementary Fig. 7).  $\text{H}_2$  was determined to be the main gaseous by-product (Supplementary Fig. 8). Notably, the FE for  $\text{NH}_2\text{OH}$  over Bi NPs/CFP reached up to 81.0% at -1.0 V vs. RHE. At -1.2 V vs. RHE, the yield rate for  $\text{NH}_2\text{OH}$  over Bi NPs/CFP was as high as  $713.1 \mu\text{mol cm}^{-2} \text{h}^{-1}$  (Fig. 4b). Such value represents the highest yield rate for  $\text{NH}_2\text{OH}$  among recent reports<sup>25-28</sup> (Supplementary Table 1). In addition, the selectivity for  $\text{NH}_2\text{OH}$  over Bi NPs/CFP was always higher than 99.3% at all applied potential. According to a series of control experiments, Bi served as the active species for the  $\text{NO}_3^-$  electroreduction into  $\text{NH}_2\text{OH}$  (Supplementary Figs. 9-11).

To evaluate the catalytic stability of Bi NPs/CFP, we carried out the continuous  $\text{NO}_3^-$  electroreduction. A 5-h continuous chronopotentiometry electrolysis at  $100 \text{ mA cm}^{-2}$  was firstly conducted to explore the accumulation of  $\text{NH}_2\text{OH}$  in the catholyte. As show in Fig. 4c, the accumulated concentrations for  $\text{NH}_2\text{OH}$  were almost linearly increased with the average yield rate for  $\text{NH}_2\text{OH}$  higher than  $456.5 \mu\text{mol cm}^{-2} \text{h}^{-1}$ . The accumulated concentration for  $\text{NH}_2\text{OH}$  reached as high as 77.7 mM (Fig. 4d). In the meantime, the FE and selectivity for  $\text{NH}_2\text{OH}$  were always higher than 73.4% and 99.3% during 5-h electrolysis, respectively (Supplementary Fig. 12). We carried out cyclic stability tests to further study the catalytic stability of Bi NPs/CFP

towards  $\text{NO}_3^-$  electroreduction. Specifically, each cycle was continuously electrolyzed at  $100 \text{ mA cm}^{-2}$  for 5 h. In the period of 12 cycles with the total electrolytic duration of 60 h, the product selectivity for  $\text{NH}_2\text{OH}$  was still higher than 99.2% (Fig. 4e). Moreover, the average yield rate for  $\text{NH}_2\text{OH}$  fluctuated within the error range of 6.0% during 12 cyclic tests. The solid  $2\text{NH}_2\text{OH}\cdot\text{H}_2\text{SO}_4$  products of 1.887 g with separation efficiency of 89.9% was achieved from the 360 mL of catholyte after 12 cyclic tests of  $\text{NO}_3^-$  electroreduction (Insert Fig. 4e). Based on the structural characterizations (Supplementary Figs. 13-16), the metallic Bi species in Bi NPs/CFP were preserved after the 60-h electrolysis.

To unravel the intrinsic reason for the high activity and selectivity for  $\text{NH}_2\text{OH}$  over Bi NPs/CFP, we investigated the reaction mechanism of  $\text{NO}_3^-$  electroreduction. Fig. 5a shows a typical pathway for the formation of  $\text{NH}_2\text{OH}$  and  $\text{NH}_3$  derived from the electroreduction of  $\text{NO}_3^-$ . Among these steps, the selectivity of the production for  $\text{NH}_2\text{OH}$  or  $\text{NH}_3$  was determined by the adsorbed behavior of  $^*\text{NH}_2\text{OH}$ . In general,  $\text{NH}_3$  has been reported as the final product for  $\text{NO}_3^-$  electroreduction over the most of metallic catalysts<sup>20,29-31</sup>. We thus adopted various metallic materials including nickel (Ni) foil, copper (Cu) foil, silver (Ag) foil, tin (Sn) foil, and platinum (Pt) foil as cathodic catalysts to uncover the formation mechanism of  $\text{NH}_2\text{OH}$  towards  $\text{NO}_3^-$  electroreduction. As shown in Fig. 5b, Bi NPs/CFP exhibited both the highest FE and yield rate for  $\text{NH}_2\text{OH}$  among all these catalysts. According to the structural characterizations, the exposed surface for the Ni foil, Cu foil, Ag foil, Sn foil, Pt foil, and Bi NPs were enclosed by cubic Ni(100), cubic Cu(100), cubic Ag(100), tetragonal Sn(211), cubic Pt(100), and hexagonal Bi(012) facets, respectively (Supplementary Fig. 17). Hence, we conducted spin polarized DFT calculations to investigate the adsorbed behaviors of  $^*\text{NH}_2\text{OH}$  by adopting representative Ni(100), Cu(100), Ag(100), Sn(211), Pt(100), and Bi(012) facets as model slabs (Supplementary Figs. 18). As shown in Fig. 5c, the Bi(012) facet displayed an  $E_{\text{ads}}$  for  $^*\text{NH}_2\text{OH}$  of 0.01 eV, much weaker than the other counterparts. This result indicated that the desorption of  $^*\text{NH}_2\text{OH}$  on Bi catalyst was more favorable in comparison with these on the other metallic catalysts. We further simulated the transformation of  $^*\text{NH}_2\text{OH}$  on the Bi(012) facet to gain in-depth understanding for the selective production of  $\text{NH}_2\text{OH}$  over Bi catalyst (Supplementary Fig. 19). As shown in Fig. 5d, the Gibbs free energy change was calculated to be -0.73 eV for the desorption of  $^*\text{NH}_2\text{OH}$  into  $\text{NH}_2\text{OH}$ , suggesting that  $^*\text{NH}_2\text{OH}$  desorption was a thermodynamically spontaneous process on the Bi(012) facet. Nevertheless, the energy barrier for  $^*\text{NH}_2\text{OH}$  dissociation into adsorbed

$\text{NH}_2$  ( $^*\text{NH}_2$ ) and adsorbed OH ( $^*\text{OH}$ ) was calculated as high as 0.85 eV on the Bi(012) facet. These results suggested that  $\text{NH}_2\text{OH}$  path was more favorable than  $\text{NH}_3$  path towards  $\text{NO}_3^-$  electroreduction over Bi catalyst. As such, the weak adsorption of  $^*\text{NH}_2\text{OH}$  was responsible for the selective formation of  $\text{NH}_2\text{OH}$  towards  $\text{NO}_3^-$  electroreduction.

## Conclusions

In summary, we developed a PECP for renewable  $\text{NH}_2\text{OH}$  electrosynthesis. Combining the plasma discharge with electroreduction processes, we significantly promoted both the  $\text{N}_2$  fixation and  $\text{NH}_2\text{OH}$  synthetic efficiency, implementing the sustainable  $\text{NH}_2\text{OH}$  synthesis from the ambient air and  $\text{H}_2\text{O}$ . During PECP, we obtained a yield rate for  $\text{NH}_2\text{OH}$  of as high as  $713.1 \mu\text{mol cm}^{-2} \text{ h}^{-1}$  with a selectivity for  $\text{NH}_2\text{OH}$  of 99.3%. We believe that the PECP for the electrosynthesis of  $\text{NH}_2\text{OH}$  could not only upgrade the  $\text{NH}_2\text{OH}$  synthetic technology but also promote N fixation. This work opens up a new route for the green and sustainable electrosynthesis of  $\text{NH}_2\text{OH}$ , which also provides rational guidelines for the renewable synthesis of other nitrogenous compounds.



## Methods

### Chemicals and materials

Concentrated sulfuric acid ( $\text{H}_2\text{SO}_4$ , 98wt%), concentrated nitric acid ( $\text{HNO}_3$ , 68wt%), ethanol (EtOH), concentrated hydrochloric acid (HCl, 37wt%), acetone, titanium (Ti) mesh, Ni foil, Cu foil, Ag foil, Sn foil, and Pt foil were purchased from Sinopharm Chemical Reagent Co., Ltd. Aqueous glyoxylic acid solution ( $\text{C}_2\text{H}_2\text{O}_3$ , 50wt%), iridium(III) chloride hexahydrate ( $\text{YCl}_3 \cdot 3\text{H}_2\text{O}$ ) were purchased from Aladdin Chemistry Co., Ltd. (Shanghai, China). Methyl sulfoxide ( $d_6$ -DMSO, 99.9atom% D), 1-Propanesulfonic acid 3-(trimethylsilyl) sodium salt (DSS), and Nafion 115 membrane were purchased from Sigma-Aldrich. Bi disk (99.995%,  $\phi 50.8 \times 3$  mm) was purchased from ZhongNuo Advanced Material (Beijing) Technology Co., Ltd. The deionized  $\text{H}_2\text{O}$  was produced using a Millipore Milli-Q grade with a resistivity of 18.2  $\text{M}\Omega \text{ cm}$ . All the chemicals were used as received without any further purification.

### Plasma synthesis of $\text{NO}_3^-$ from the ambient air and $\text{H}_2\text{O}$

In the standard plasma synthetic process, the ambient air with controllable flow rates was pumped into the homemade plasma discharge device. A high-voltage generator was adopted as power supply with the input AC voltage and power of 50 V and 20 W, respectively. During the plasma synthetic process, the as-obtained  $\text{NO}_x$  were absorbed by a homemade absorption tower using deionized  $\text{H}_2\text{O}$  as the absorbent. The concentration of  $\text{NO}_3^-$  after the absorption of  $\text{NO}_x$  was quantitatively analyzed by ion chromatography.

### Synthesis of Bi NPs/CFP

The Bi NPs/CFP was synthesized based on our previous report with a slight modification<sup>32</sup>. Typically, Bi disk and CFP were used as target material and substrate, respectively. Direct current magnetron sputtering was conducted with a constant current of 50 mA under an Ar atmosphere ( $2.4 \times 10^{-3}$  mbar, 20 SCCM) at room temperature for 3000 s. After the magnetron sputtering process, the as-obtained sample was directly used as the catalyst for  $\text{NO}_3^-$  electroreduction measurements.

### Pretreatment of metallic foils

Ni foil, Cu foil, Ag foil, Sn foil, and Pt foil were immersed in EtOH and ultrasonically cleaned for at least 10 min. EtOH was then replaced by acetone to conduct the ultrasonic cleaning process. After three repeated treatments, the working electrodes were immersed in 10wt% of HCl solution for 10 min to remove surface oxide. After HCl treatment, the working electrodes were washed with deionized H<sub>2</sub>O and stored in acetone for further use.

### **NO<sub>3</sub><sup>-</sup> electroreduction measurements**

The NO<sub>3</sub><sup>-</sup> electroreduction measurements were carried out in a conventional H cell, in which anolyte (30 mL of 0.5 M H<sub>2</sub>SO<sub>4</sub>) and catholyte (30 mL of 0.5 M H<sub>2</sub>SO<sub>4</sub> mixed with 0.1 M HNO<sub>3</sub>) were separated by Nafion 115 membrane. Bi NPs/CFP, IrO<sub>2</sub> loaded Ti mesh, and Ag/AgCl were used as working electrode, counter electrode, and reference electrode, respectively. The chronoamperometry electrolysis was controlled by an Autolab potentiostat/galvanostat (CHI660E). All potentials were measured vs. the Ag/AgCl reference electrode (vs. Ag/AgCl) and converted to the reversible hydrogen electrode reference scale (vs. RHE) without iR correction on account of the equation:  $E \text{ (vs. RHE)} = E \text{ (vs. Ag/AgCl)} + 0.21 \text{ V} + 0.0591 \times \text{pH}$ . During the process of NO<sub>3</sub><sup>-</sup> electroreduction, the gaseous products in Ar stream were monitored by an online GC equipped with a flame ionization detector and a thermal conductivity detector once every five minutes. The liquid products were detected by <sup>1</sup>H NMR, where NH<sub>2</sub>OH was captured by an excess amount of C<sub>2</sub>H<sub>2</sub>O<sub>3</sub> through oximation. Specifically, 0.4 mL of the catholyte after 1-h electrolysis was mixed with 0.1 mL of *d*<sub>6</sub>-DMSO and 12.5 μL of 50wt% C<sub>2</sub>H<sub>2</sub>O<sub>3</sub>. 0.1 mL of 6.0 mM DSS solution was added as an internal standard. The chronopotentiometry electrolysis at 100 mA cm<sup>-2</sup> (corresponding to -1.0 V vs. RHE) was conducted for both the continuous NO<sub>3</sub><sup>-</sup> electroreduction and cyclic stability tests.

### **The calculation of FE**

The FE for a specific product was calculated according to equation 1:

$$\text{FE} = C_{\text{product}} \times V \times N \times F / Q \times 100\% \quad (1)$$

$C_{\text{product}}$ : the measured concentration of a specific product, mole per liter (mol/L, M);

$V$ : the volume of the electrolyte for liquid products and the total gaseous volume for gaseous products, liter (L);

N: the number of electron transfer for the formation of a specific product, 6, 8, and 2 for the formation of  $\text{NH}_2\text{OH}$ ,  $\text{NH}_3$ , and  $\text{H}_2$ , respectively;

$F$ : Faraday constant,  $96485 \text{ C mol}^{-1}$ ;

$Q$ : quantity of electric charge, coulomb (C).

### The calculation of the yield rate for $\text{NH}_2\text{OH}$

The yield rate for  $\text{NH}_2\text{OH}$  was calculated based on the following equation:

$$\text{yield rate}(\text{NH}_2\text{OH}) = n(\text{NH}_2\text{OH})/A/t \quad (2)$$

$n$ : the accumulated molar quantity during  $t$ -h  $\text{NO}_3^-$  electroreduction,  $10^{-6}$  mole ( $\mu\text{mol}$ );

$A$ : the geometric area of the cathodic electrode, square centimeter ( $\text{cm}^2$ );

$t$ : reaction time, hour (h).

### The calculation of selectivity for $\text{NH}_2\text{OH}$

The selectivity for  $\text{NH}_2\text{OH}$  was calculated according to equation 3:

$$\text{Selectivity}(\text{NH}_2\text{OH}) = n(\text{NH}_2\text{OH})/[n(\text{NH}_2\text{OH})+n(\text{NH}_3)] \times 100\% \quad (3)$$

$n$ : the accumulated molar quantity during a period of  $\text{NO}_3^-$  electroreduction,  $\mu\text{mol}$ .

### DFT calculations

Spin-polarized periodic DFT calculations were performed using the Vienna Ab-Initio Simulation Package (VASP) code at the GGA level within the PAW-PBE formalism<sup>33-36</sup>. The van der Waals interactions were described using the empirical DFT+D3 method<sup>37</sup>. The slab models of the four-layer Ni(100) facet, four-layer Cu(100) facet, four-layer Ag(100) facet, four-layer Sn(211) facet, four-layer Pt(100) facet, and two-layer Bi(012) facet were adopted with a vacuum of  $15 \text{ \AA}$ . The total energy calculations were performed using a  $3 \times 3 \times 1$  grid and a plane wave with cut-off energy of 400 eV. Atoms in the bottom two layers were fixed and all other atoms including adsorbates were allowed to relax until the force on each ion was smaller than  $0.02 \text{ eV \AA}^{-1}$ .

The  $E_{\text{ads}}$  was defined as follow:

$$E_{\text{ads}} = E_{\text{adsorb-surf}} - E_{\text{surf}} - E_{\text{adsorb}} \quad (4)$$

where  $E_{\text{adsorb-surf}}$ ,  $E_{\text{surf}}$ , and  $E_{\text{adsorb}}$  represent the total energies of the slab with adsorbate, the clean slab, and the isolated adsorbate, respectively.

The Gibbs free energy change is defined as follow:

$$\Delta G = \Delta E + \Delta ZPE - T\Delta S \quad (5)$$

where  $\Delta E$  is obtained from DFT calculations,  $\Delta ZPE$  represents the correction in zero-point energies, and  $T\Delta S$  is the contribution of entropy. In this study, we use the nudged elastic band (NEB) method<sup>37</sup> to calculate the activation energy for the breaking of N-O bonds in \*NH<sub>2</sub>OH.

## Instrumentations

SEM images and EDX elemental mapping images were obtained with a scanning electron microscope (SEM, JSM-6700F) operated at 5 kV. HAADF-STEM images were carried out on a JEOL ARM-200F field-emission transmission electron microscope operating at an accelerating voltage of 200 kV using Cu-based TEM grids. XRD patterns were recorded by using a Philips X'Pert Pro Super diffractometer with Cu- $K_\alpha$  radiation ( $\lambda = 1.54178 \text{ \AA}$ ). XPS measurements were performed on a Kratos Axis Supra<sup>+</sup> X-ray photoelectron spectrometer with an exciting source of Al  $K_\alpha = 1486.6 \text{ eV}$ . The gaseous products were monitored by an online gas chromatography (SHIMADZU, GC-2014). Liquid products were examined on a Varian 400 MHz NMR spectrometer (Bruker AVANCE AV III 400). The concentration of NO<sub>3</sub><sup>-</sup> was quantitatively determined *via* an ion chromatography (Thermo Scientific, DIONES AX-DV). Raman spectroscopy measurements were carried out on a LabRAM HR Evolution (HORIBA Scientific).

## Data Availability

All data that led us to understand the results presented here are available with the paper or from the corresponding author upon reasonable request.

## References

1. Rosca, V., Duca, M., de Groot, M. T. & Koper, M. T. M. Nitrogen cycle electrocatalysis. *Chem. Rev.* **109**, 2209-2244 (2009).
2. Tabolin, A. A. & Ioffe, S. L. Rearrangement of N-oxyenamines and related reactions. *Chem. Rev.* **114**, 5426-5476 (2014).
3. Huang, H., Ji, X., Wu, W. & Jiang, H. Transition metal-catalyzed C-H functionalization of N-oxyenamine internal oxidants. *Chem. Soc. Rev.* **44**, 1155-1171 (2015).
4. Zhao, F. et al. A simple and efficient approach for preparation of hydroxylamine sulfate from the acid-catalyzed hydrolysis reaction of cyclohexanone oxime. *Chem. Eng. J.* **272**, 102-107 (2015).
5. Manente, F., Pietrobon, L., Ronchin, L. & Vavasori, A. Trifluoroacetic acid hydroxylamine system as organocatalyst reagent in a one-pot salt free process for the synthesis of caprolactam and amides of industrial interest. *Catal. Lett.* **151**, 3543-3549 (2021).
6. Tursun, M. & Wu, C. Single transition metal atoms anchored on defective MoS<sub>2</sub> monolayers for the electrocatalytic reduction of nitric oxide into ammonia and hydroxylamine. *Inorg. Chem.* **61**, 17448-17458 (2022).
7. Semon, W. L. The preparation of hydroxylamine hydrochloride and acetoxime. *J. Am. Chem. Soc.* **45**, 188-190 (1923).
8. Tauszik, G. R. & Crocetta, P. Production of hydroxylamine from nitrogen oxide: A short review. *Appl. Catal.* **17**, 1-21 (1985).
9. Benson, R. E., Cairns, T. L. & Whitman, G. M. Synthesis of hydroxylamine. *J. Am. Chem. Soc.* **78**, 4202-4205 (1956).
10. Shelef, M. & Graham, G. W. Why rhodium in automotive three-way catalysts? *Catal. Rev.* **36**, 433-457 (1994).
11. Murray, R. W. & Singh, M. A high yield one step synthesis of hydroxylamines. *Synth. Commun.* **19**, 3509-3522 (1989).
12. Mantegazza, M. A. & Leofanti, G. A one-step rapid synthesis of TS-1 zeolites with highly catalytically active mononuclear TiO<sub>6</sub> species. *Stud. Surf. Sci. Catal.* **82**, 541-550 (1994).
13. Tsegaw, Y. A. et al. Formation of hydroxylamine in low-temperature interstellar model ices. *J. Phys. Chem. A* **121**, 7477-7493 (2017).
14. Zecchina, A. et al. Structural characterization of Ti centres in Ti-silicalite and reaction

- mechanisms in cyclohexanone ammoximation. *Catal. Today* **32**, 97-106 (1996).
15. Wu, P., Komatsu, T. & Yashimal, T. Ammoximation of ketones over titanium mordenite. *J. Catal.* **168**, 400-411 (1997).
  16. Wu, Y., Jiang, Z., Lin, Z., Liang, Y. & Wang, H. Direct electrosynthesis of methylamine from carbon dioxide and nitrate. *Nat. Sustain.* **4**, 725-730 (2021).
  17. Liu, X., Jiao, Y., Zheng, Y., Jaroniec, M. & Qiao, S. Z. Mechanism of C-N bonds formation in electrocatalytic urea production revealed by ab initio molecular dynamics simulation. *Nat. Commun.* **13**, 5471 (2022).
  18. Zheng, T. et al. Upcycling CO<sub>2</sub> into energy-rich long-chain compounds via electrochemical and metabolic engineering. *Nat. Catal.* **5**, 388-396 (2022).
  19. Chen, G.-F. et al. Electrochemical reduction of nitrate to ammonia via direct eight-electron transfer using a copper-molecular solid catalyst. *Nat. Energy* **5**, 605-613 (2020).
  20. Chen, F.-Y. et al. Efficient conversion of low-concentration nitrate sources into ammonia on a Ru-dispersed Cu nanowire electrocatalyst. *Nat. Nanotechnol.* **17**, 759-767 (2022).
  21. Liu, Y. et al. A highly efficient metal-free electrocatalyst of F-doped porous carbon toward N<sub>2</sub> electroreduction. *Adv. Mater.* **32**, e1907690 (2020).
  22. Winter, L. R. & Chen, J. G. N<sub>2</sub> fixation by plasma-activated processes. *Joule* **5**, 300-315 (2021).
  23. Ren, Y. et al. Microscopic-level insights into the mechanism of enhanced NH<sub>3</sub> synthesis in plasma-enabled cascade N<sub>2</sub> oxidation-electroreduction system. *J. Am. Chem. Soc.* **144**, 10193-10200 (2022).
  24. Li, L. et al. Efficient nitrogen fixation to ammonia through integration of plasma oxidation with electrocatalytic reduction. *Angew. Chem. Int. Ed.* **60**, 14131-14137 (2021).
  25. Daems, N., Sheng, X., Alvarez-Gallego, Y., Vankelecom, I. F. J. & Pescarmona, P. P. Iron-containing N-doped carbon electrocatalysts for the cogeneration of hydroxylamine and electricity in a H<sub>2</sub>-NO fuel cell. *Green Chem.* **18**, 1547-1559 (2016).
  26. Sheng, X. et al. Carbon-supported iron complexes as electrocatalysts for the cogeneration of hydroxylamine and electricity in a NO-H<sub>2</sub> fuel cell: A combined electrochemical and density functional theory study. *J. Power Sources* **390**, 249-260, (2018).
  27. Kim, D. H. et al. Selective electrochemical reduction of nitric oxide to hydroxylamine by atomically dispersed iron catalyst. *Nat. Commun.* **12**, 1856 (2021).

28. Zhang, X. et al. Direct electro-synthesis of valuable C=N compound from NO. *Chem Catal.* **2**, 1807-1818 (2022).
29. Wang, Y. et al. Enhanced nitrate-to-ammonia activity on copper–nickel alloys via tuning of intermediate adsorption. *J. Am. Chem. Soc.* **142**, 5702-5708 (2020).
30. Song, Z. et al. Efficient electroreduction of nitrate into ammonia at ultralow concentrations via an enrichment effect. *Adv. Mater.* **34**, 2204306 (2022).
31. Ye, S. et al. Elucidating the activity, mechanism and application of selective electrosynthesis of ammonia from nitrate on cobalt phosphide. *Energy Environ. Sci.* **15**, 760 (2022).
32. Kong, X. et al. Enhancing CO<sub>2</sub> electroreduction selectivity toward multicarbon products via tuning the local H<sub>2</sub>O/CO<sub>2</sub> molar ratio. *Nano Lett.* **22**, 8000-8007 (2022).
33. Kresse, G. & Furthmüller, J. Efficiency of ab-initio total energy calculations for metals and semiconductors using a plane-wave basis set. *Comput. Mater. Sci.* **6**, 15-50 (1996).
34. Kresse, G. & Joubert, D. From ultrasoft pseudopotentials to the projector augmented-wave method. *Phys. Rev. B* **59**, 1758-1775 (1999).
35. Perdew, J. P., Burke, K. & Ernzerhof, M. Generalized gradient approximation made simple. *Phys. Rev. Lett.* **77**, 3865-3868 (1996).
36. Grimme, S., Ehrlich, S. & Goerigk, L. Effect of the damping function in dispersion corrected density functional theory. *J. Comp. Chem.* **32**, 1456 (2011).
37. Henkelman, G., Uberuaga, B. P. & Jonsson, H. A climbing image nudged elastic band method for finding saddle points and minimum energy paths. *J. Chem. Phys.* **113**, 9901-9904 (2000).

## ACKNOWLEDGMENTS

**Funding:** This work was supported by National Key Research and Development Program of China (2021YFA1500500 and 2022YFC2106000), Strategic Priority Research Program of the Chinese Academy of Sciences (XDB0450401), CAS Project for Young Scientists in Basic Research (YSBR-051 and YSBR-022), National Science Fund for Distinguished Young Scholars (21925204), National Natural Science Foundation of China (92061111, U19A2015, 22221003, 22250007, and 22209163), Fundamental Research Funds for the Central Universities, Provincial Key Research and Development Program of Anhui (202004a05020074), Collaborative

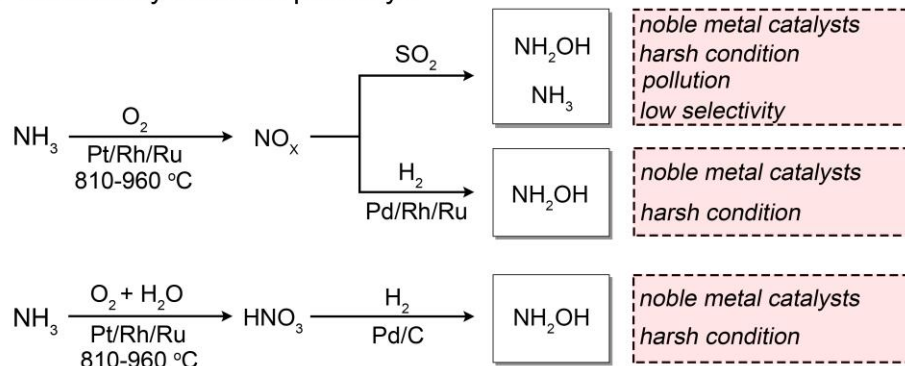
Innovation Program of Hefei Science Center, CAS (2022HSC-CIP004), the Joint Fund of the Yulin University and the Dalian National Laboratory for Clean Energy (YLU-DNL Fund 2022012), K. C. Wong Education (GJTD-2020-15), the DNL Cooperation Fund, CAS (DNL202003), Youth Project of Anhui Natural Science Foundation (2208085QB43), and USTC Research Funds of the Double First-Class Initiative (YD2340002002). This work was partially carried out at the USTC Center for Micro and Nanoscale Research and Fabrication.

**Author contributions:** X.K. and J.N. contributed equally to this work. J.Z., Z.G., and X.K. conceived the idea and co-wrote the paper. X.K. and J.N. synthesized catalysts, conducted structural characterizations, and performed electroreduction tests with the help of J.Zheng and Z.X.. Z.S. and X.K. designed the plasma discharge device and performed the N<sub>2</sub> plasma fixation tests with the help of L.Q.. Z.Y. performed the theoretical calculations. H.L. made suggestions on the paper. All authors discussed the results and commented on the manuscript.

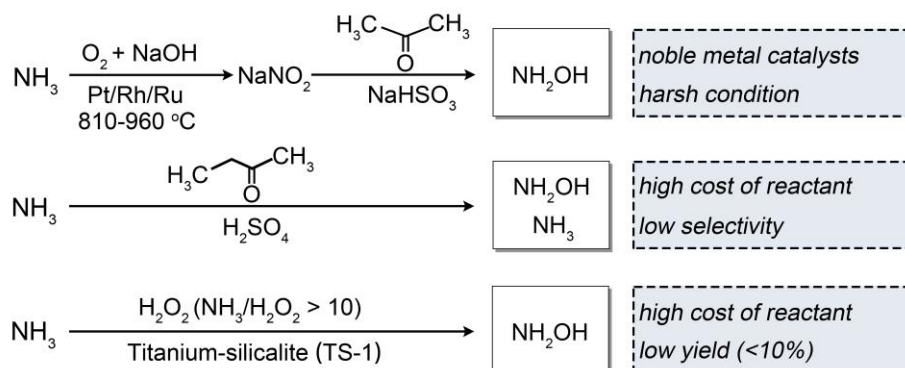
**Competing interests:** The authors declare no financial interests.



**a** Traditionally industrial pathways



**b** Newly emerging pathways



**c** Plasma-electrochemical cascade pathway (this work)

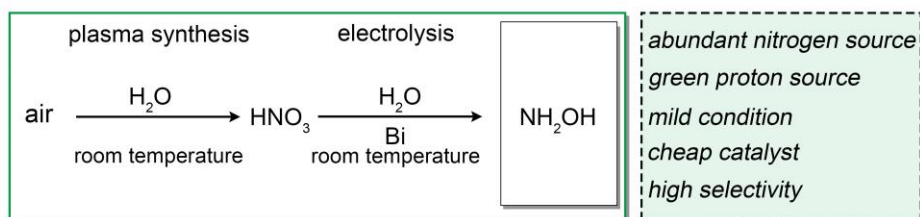


**Fig. 1 | Schematic illustration of the synthetic pathways for NH<sub>2</sub>OH.** **a-c**, The traditionally industrial pathways (**a**), the newly emerging pathways (**b**), and the sustainable PECP from the ambient air and H<sub>2</sub>O (**c**).

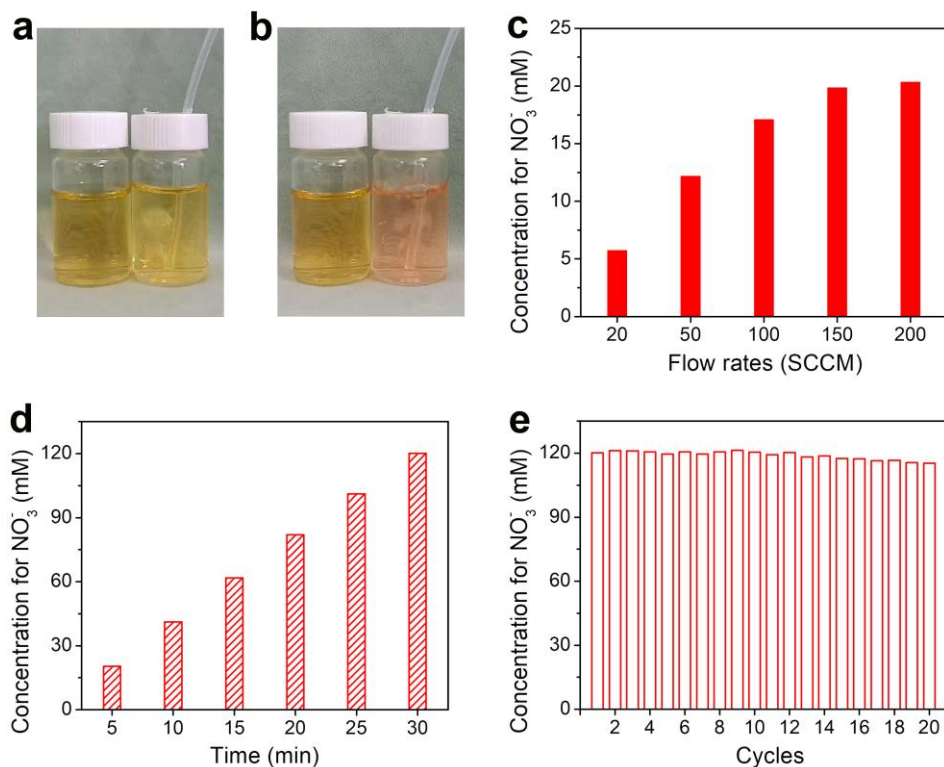


**Fig. 2 | Plasma synthesis of  $\text{NO}_3^-$  from the ambient air and  $\text{H}_2\text{O}$ .** **a,b**, The photographs of the pristine absorbent (**a**) and the absorbent after absorbing the gaseous substances produced by the plasma discharge device for 30 s (**b**). The vials on the left and right sides were used as control and experiment groups, respectively. **c**, The concentration for  $\text{NO}_3^-$  in 30 mL of absorbent under various flow rates of ambient air for a 5-min discharge. **d**, The accumulated concentration for  $\text{NO}_3^-$  in 30 mL of absorbent under the flow rate of 200 SCCM for various discharge times. **e**, Cyclic stability for  $\text{NO}_3^-$  production in 30 mL of absorbent under the flow rate of 200 SCCM with each cycle for a 30-min continuous discharge.

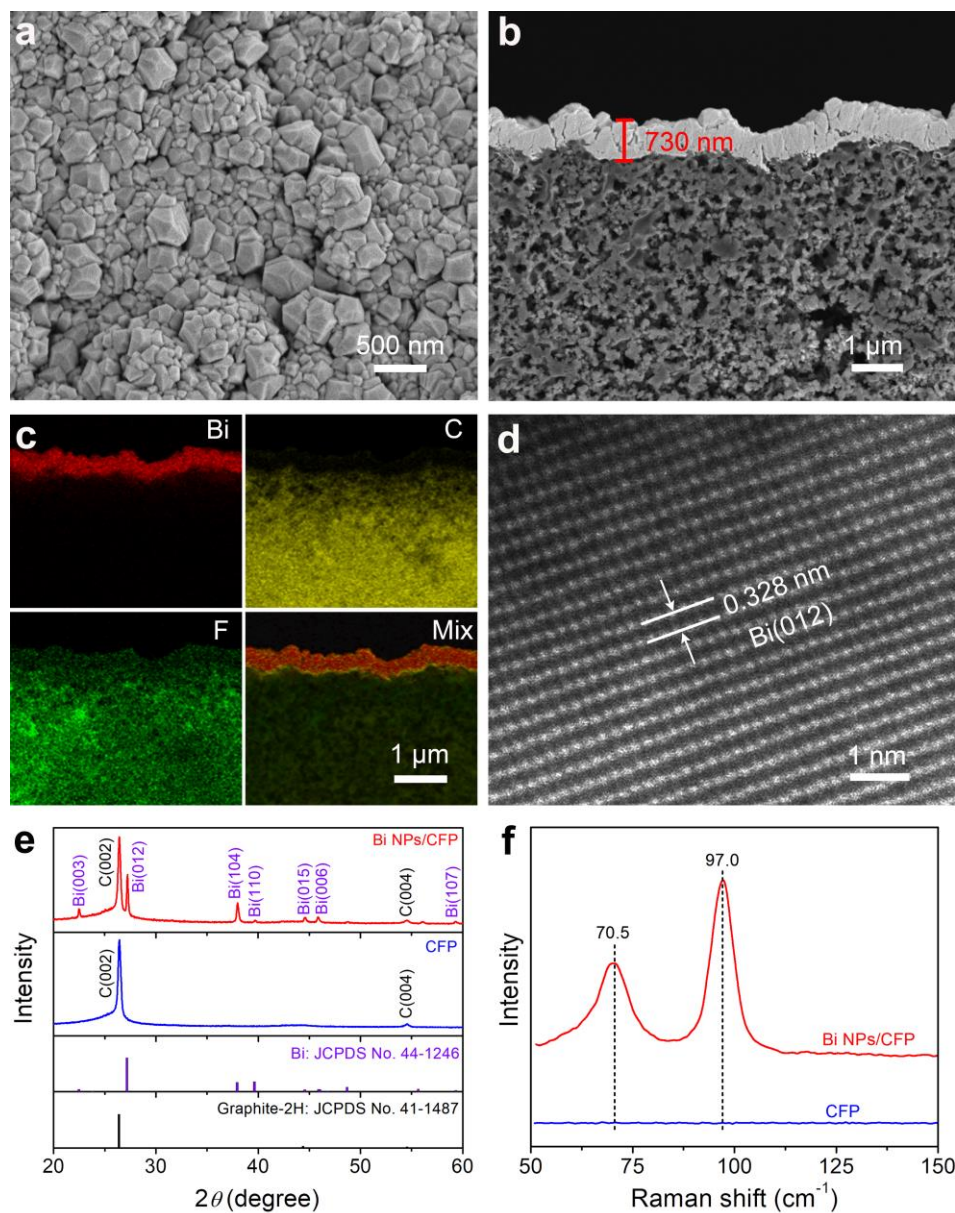


**Fig. 3 | Characterizations of Bi NPs/CFP catalyst.** **a**, SEM image of Bi NPs/CFP. **b,c**, SEM image (**b**) and SEM-EDX elemental mapping images (**c**) of the cross-sectional Bi NPs/CFP. **d**, HAADF-STEM image of an individual Bi nanoparticle in Bi NPs/CFP. **e,f**, XRD patterns (**e**) and Raman spectra (**f**) of both Bi NPs/CFP and CFP.

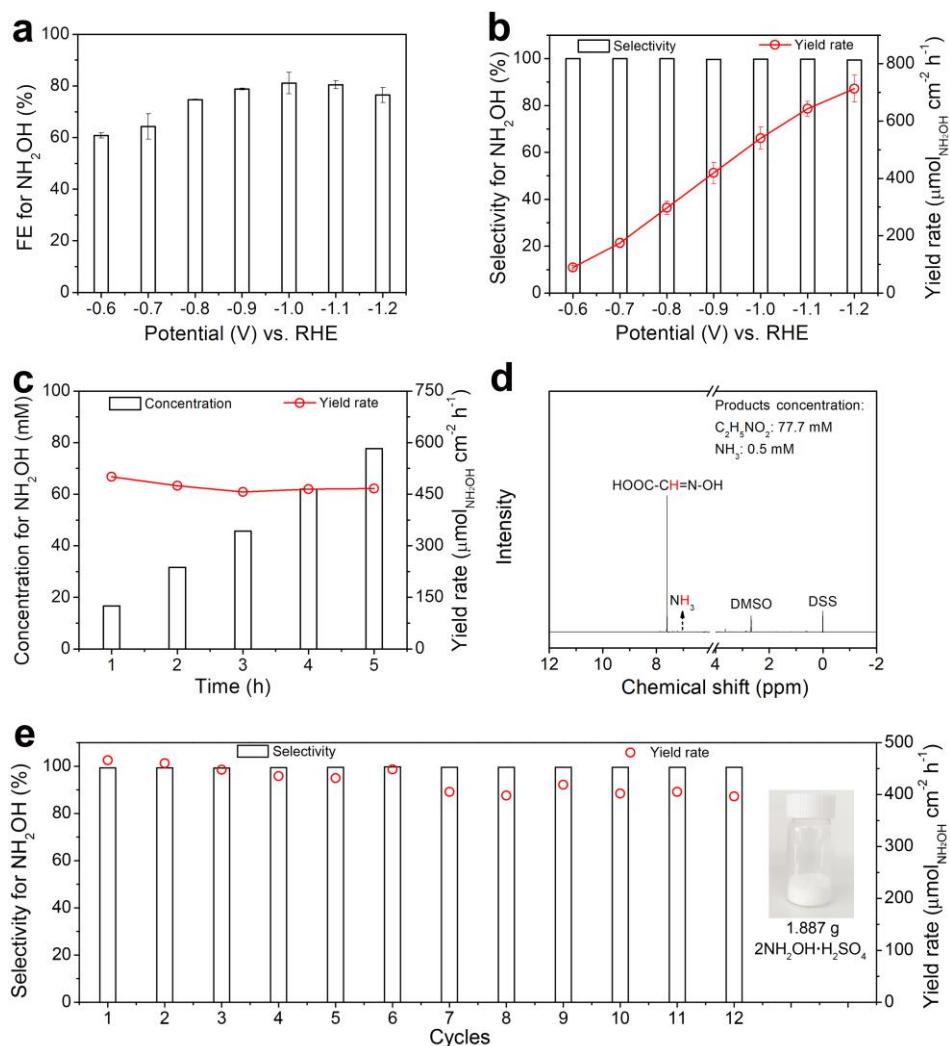


**Fig. 4 | Catalytic performance of  $\text{NO}_3^-$  electroreduction over Bi NPs/CFP.** **a,b**, FE for  $\text{NH}_2\text{OH}$  (**a**) and the selectivity/yield rate for  $\text{NH}_2\text{OH}$  (**b**) towards  $\text{NO}_3^-$  electroreduction over Bi NPs/CFP. **c**, The accumulated concentration and yield rate for  $\text{NH}_2\text{OH}$  during the 5-h continuous electrolysis. **d**,  $^1\text{H}$  NMR spectrum of the electrolyte after the 5-h continuous electrolysis with the addition of 0.2 M  $\text{C}_2\text{H}_2\text{O}_3$ . **e**, Cyclic stability test towards  $\text{NO}_3^-$  electroreduction over Bi NPs/CFP with each cycle for a 5-h continuous electrolysis. Insert Fig. 4e shows the solid  $2\text{NH}_2\text{OH} \cdot \text{H}_2\text{SO}_4$  products separated after 12 cyclic tests of  $\text{NO}_3^-$  electroreduction.

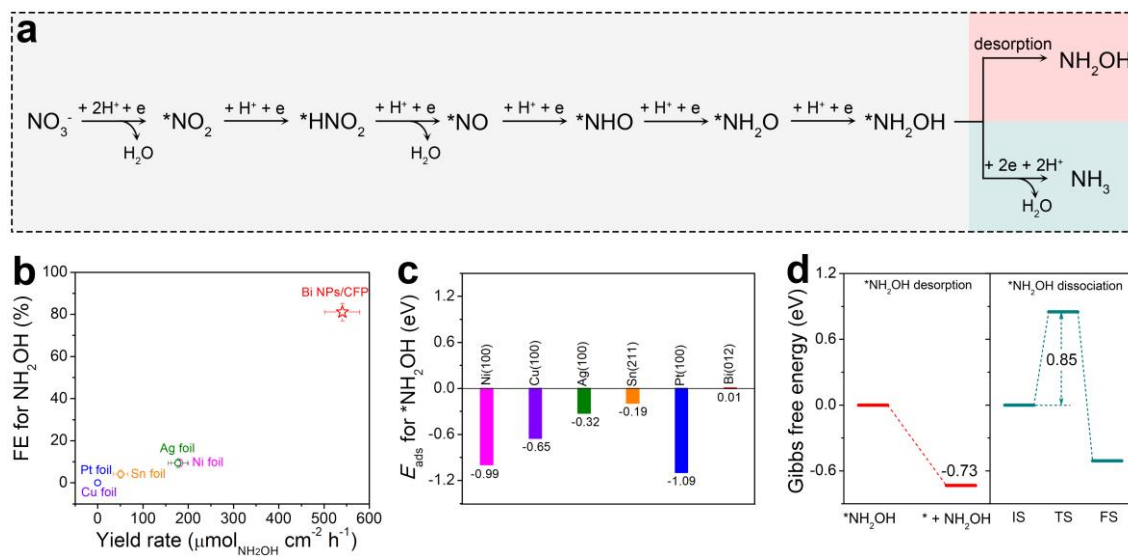


**Fig. 5 | Mechanistic study of  $\text{NO}_3^-$  electroreduction into  $\text{NH}_2\text{OH}$ .** **a**, A typical reaction pathway for  $\text{NH}_2\text{OH}$  and  $\text{NH}_3$  towards  $\text{NO}_3^-$  electroreduction. **b**, FE for  $\text{NH}_2\text{OH}$  plotted against yield rate for  $\text{NH}_2\text{OH}$  over various metallic catalysts at -1.0 V vs. RHE. **c**,  $E_{\text{ads}}$  for  $\text{*NH}_2\text{OH}$  on various metallic surfaces. **d**, Gibbs free energy diagram for  $\text{*NH}_2\text{OH}$  desorption and  $\text{*NH}_2\text{OH}$  dissociation on the Bi(012) facet.